Electronic Spectroscopy and Dissociation Dynamics of Vinyl-Substituted Criegee Intermediates: 2-Butenal Oxide and Comparison with Methyl Vinyl Ketone Oxide and Methacrolein Oxide Isomers

Guanghan Wang,[1†] Tianlin Liu,[1†] Meijun Zou,[1] Christopher A. Sojdak,[1] Marisa C. Kozlowski,[1]
Tolga N. V. Karsili,[2] and Marsha I. Lester[1*]

[1] Department of Chemistry, University of Pennsylvania, Philadelphia, PA 19104-6323 USA
[2] Department of Chemistry, University of Louisiana at Lafayette, Lafayette, LA 70504 USA

Abstract

The 2-butenal oxide Criegee intermediate [$(CH_3CH=CH)CHOO$], an isomer of the four-carbon unsaturated Criegee intermediates derived from isoprene ozonolysis, is characterized on its first $\pi^*\leftarrow\pi$ electronic transition and by the resultant dissociation dynamics to O (^1D) + 2-butenal [$(CH_3CH=CH)CHO$] products. The electronic spectrum of 2-butenal oxide under jet-cooled conditions is observed to be broad and unstructured with peak absorption at 373 nm, spanning to half maxima at 320 and 420 nm, and in good accord with the computed vertical excitation energies and absorption spectra obtained for its lowest energy conformers. The distribution of total kinetic energy released to products is ascertained through velocity map imaging of the O (^1D) products. About half of the available energy, deduced from the theoretically computed asymptotic energy, is accommodated as internal excitation of the 2-butenal fragment. A reduced impulsive model is introduced to interpret the photodissociation dynamics, which accounts for the geometric changes between 2-butenal oxide and the 2-butenal fragment, and vibrational activation of associated modes in the 2-butenal product. Application of the reduced impulsive model to the photodissociation of isomeric methyl vinyl ketone oxide reveals greater internal activation of the methyl vinyl ketone product arising from methyl internal rotation and rock, which is distinctly different than the dissociation dynamics of 2-butenal oxide or methacrolein oxide.

[†] Equal contributions.

[*] Corresponding author email: milester@sas.upenn.edu

1. Introduction

Alkenes originating from biogenic and anthropogenic sources are the most abundant non-methane volatile organic compounds emitted into the atmosphere.[1] Ozonolysis, a significant tropospheric removal pathway for alkenes,[2, 3] proceeds via cycloaddition of ozone across the C=C double bond to form a primary ozonide, which fragments into a zwitterionic carbonyl oxide ($R_1R_2C{=}O^+O^-$ with R_1, R_2 substituents), known as the Criegee intermediate, and carbonyl products.[4] The Criegee intermediates are initially formed with high internal energy and can undergo rapid unimolecular decay or collisional stabilization, the latter followed by thermal unimolecular decay and/or bimolecular reaction with atmospheric species such as water vapor, formic acid, and SO_2.[5] Unimolecular decay of Criegee intermediates is a significant source of hydroxyl (OH) radicals,[6-9] while their bimolecular reactions are implicated in secondary organic aerosol formation and thereby impact on climate.[10, 11]

Isoprene is the most abundant alkene emitted into the atmosphere with ca. 10% loss due to ozonolysis.[12] Ozonolysis of isoprene yields formaldehyde oxide (CH_2OO), methyl vinyl ketone oxide [$(CH_2{=}CH)(CH_3)COO$, MVK-oxide], and methacrolein oxide [$(CH_2{=}C(CH_3))CHOO$, MACR-oxide] Criegee intermediates.[12] Ozonolysis of 1,3-pentadiene and other branched diolefins can yield 2-butenal oxide [$(CH_3CH{=}CH)CHOO$],[13] which is an isomer of MVK-oxide and MACR-oxide. These four-carbon Criegee intermediates have vinyl and methyl substituents, but differ in the position of the methyl group as shown in Scheme 1.[12] In MVK-oxide, the methyl group is bound to the carbonyl carbon, while in MACR-oxide or 2-butenal oxide, the methyl group is attached to the α- or β-site of the vinyl group. These Criegee intermediates have extended conjugation involving six π electrons across the vinyl (C=C) and carbonyl oxide ($C{=}O^+O^-$) functional groups. The vinyl side chain resonantly stabilizes the carbonyl oxide group and influences many properties of the Criegee intermediates, including their electronic spectra,[14, 15] unimolecular decay dynamics,[13, 16, 17] and bimolecular chemistry.[16, 18-22]

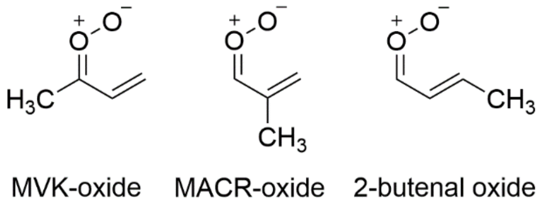

Scheme 1. Chemical structures of structurally similar Criegee intermediates with methyl and vinyl substituents, noting that each has multiple low energy conformers.

2-butenal oxide is predicted to have eight conformers (optimized geometries shown in Supporting Information, SI, Figure S1) with ground state energies that differ by up to 6.1 kcal mol^{-1} as illustrated in the disconnectivity diagram of Figure 1. The eight conformers of 2-butenal oxide can be grouped into four pairs based on the orientation of the carbonyl oxide group (first *E* or *Z*) and the vinyl group (second *E* or *Z*), labeled as *EE*, *ZE*, *EZ*, and *ZZ*. Each pair of *E*/*Z* conformers are separated by high barriers of ca.

25 kcal mol^{-1} or ca. 35 kcal mol^{-1} associated with internal rotation about the C=O or C=C double bond, respectively. Within each *E*/*Z* pair, the conformers can be further distinguished as *cis* (*c*) or *trans* (*t*), referring to the relative orientation of the carbonyl oxide and vinyl groups. The *c*/*t* conformers are connected by internal rotation about a C−C single bond via relatively low barriers of ca. 10 kcal mol^{-1}.[13, 16]

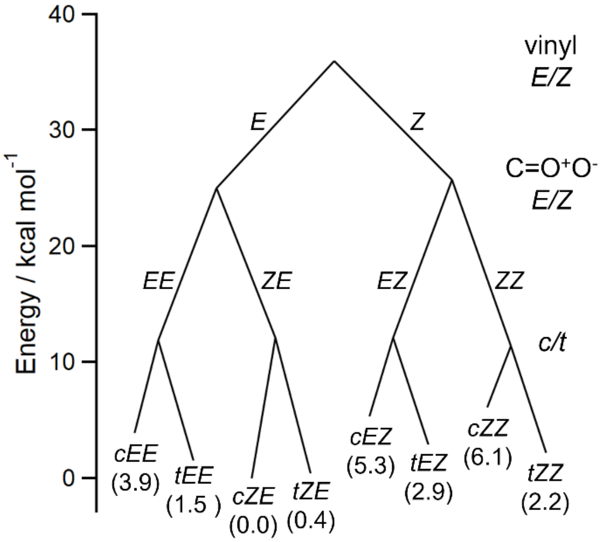

Figure 1. Disconnectivity diagram for the 2-butenal oxide Criegee intermediate, showing the eight conformers and the interconversion barriers (vinyl E/Z, C=O$^+$O$^-$ E/Z, or c/t) that separate them.[13]

Recently, this laboratory demonstrated that 248 nm photolysis of a 1,3-diiodobut-1-ene precursor forms a resonance-stabilized monoiodoalkene radical, which reacts with O_2 to generate the 2-butenal oxide Criegee intermediate (Scheme S1).[13] This laboratory synthetic route is analogous to that used to generate MVK-oxide and MACR-oxide previously.[23, 24] The nascent 2-butenal oxide is expected to be internally excited (ca. 50 kcal mol^{-1}), as found for MVK-oxide and MACR-oxide,[25, 26] providing sufficient energy for interconversion among conformers prior to thermalization. Thus far, jet-cooled and isolated 2-butenal oxide (ca. 10 K) has been investigated by infrared (IR) action spectroscopy with detection of OH products arising from unimolecular decay.[13] Upon IR activation at ca. 3000 cm^{-1}, a lower-energy *tZZ* conformer was shown to undergo prompt *c*↔*t* isomerization to the higher-energy *cZZ* conformer, followed by rapid unimolecular decay (< 5 ns) via allylic 1,6 H-atom transfer to release OH products (Scheme S2). The higher-energy *cZZ* conformer was not directly detected by IR action spectroscopy, indicating its lower population likely due to rapid unimolecular decay. The associated thermal unimolecular decay rate is predicted to be exceedingly fast at ca. 10^6 s^{-1} (298 K, 1 bar), which is five orders of magnitude faster than thermal decay of alkyl-substituted Criegee intermediates by the typical 1,4 H-atom transfer mechanism.[13, 16]

2-butenal oxide may undergo a wide range of unimolecular decay processes.[13, 16] These include rapid *c*↔*t* isomerization to the lower-energy conformer with thermal rates (298 K, 1 bar) on the order of 10^5 to

10^6 s^{-1}. Other decay processes include 1,5-ring closure to dioxole (Scheme S3), observed previously for *anti*-MVK-oxide and *syn*-MACR-oxide,[17] which is predicted to occur with a thermal decay rate of ca. 10^3 s^{-1} (298 K, 1 atm).[16, 17, 23] This decay pathway is accessible to the *ZE* and *ZZ* conformers of 2-butenal oxide, and results in subsequent isomerization to epoxide and/or β-dicarbonyl products along with its enolic tautomers (Schemes S3 and S4).[16, 17, 23] In addition, *EE* and *EZ* conformers can undergo 1,3-ring closure to dioxirane (Scheme S5) with thermal decay rates of ca. 10^2 s^{-1} (298 K, 1 atm). This study focuses on the lowest energy conformers of 2-butenal oxide, primarily *cZE*, and *tZE*, *tEE*, and *tZZ*.

Previously, this laboratory reported the electronic spectra of MVK-oxide and MACR-oxide on the first $\pi^* \leftarrow \pi$ transition under jet-cooled conditions,[24, 27] revealing a significant spectral shift to longer wavelength than found for CH_2OO or alkyl substituted Criegee intermediates.[15, 28-35] The spectral shift was attributed to extended π conjugation across the carbonyl oxide and the vinyl groups. Additional photodissociation experiments demonstrated that electronic excitation of MVK-oxide or MACR-oxide to the first $^1\pi\pi^*$ state results in prompt release of O (^{1}D) products and a high degree of internal excitation of the methyl vinyl ketone [$(CH_2{=}CH)(CH_3)CO$, MVK] or methacrolein [$(CH_2{=}C(CH_3))CHO$, MACR] co-products.

This study presents the first experimental and theoretical examination of the electronic spectroscopy of 2-butenal oxide, and introduces a reduced impulsive model for interpretation of the resultant photodissociation dynamics to O (^{1}D) + 2-butenal [$(CH_3CH{=}CH)CHO$]. The results are compared with prior studies of isomeric MVK-oxide and MACR-oxide, providing new insights on the properties of Criegee intermediates with extended conjugation.

2. Methods

2.1 Experimental

Synthesis of the (*Z/E*)-1,3-diiodobut-1-ene precursor and generation of the 2-butenal oxide Criegee intermediate were described previously.[13] Additional details are shown in Scheme S1. In this study, the diiodoalkene precursor is heated to 35 °C, entrained in a 20% O_2/Ar carrier gas mixture (10 psi), and pulsed through a nozzle (Parker-Hannifin General Valve, 1 mm orifice) into a quartz capillary tube reactor (1 mm ID, ~25 mm length) at 10 Hz. The precursor is photolyzed near the exit of the quartz tube using the cylindrically focused 248 nm output from a KrF excimer laser (Coherent, Compex 102, ~30 mJ pulse^{-1}, 10 Hz), which induces the first C-I bond dissociation. Subsequent reaction with O_2 produces the 2-butenal oxide Criegee intermediate, which is collisionally stabilized and cooled in a supersonic expansion to a rotational temperature of ~10 K.[36, 37] The gas mixture travels ~4 cm downstream (~90 μs) to a collision-free interaction region, where two types of experiments are conducted.

In the first type of experiment, the electronic spectrum of 2-butenal oxide is obtained by a UV-visible (UV-vis) induced depletion method using a time-of-flight mass spectrometer (TOF-MS) as described previously.[15, 24, 27, 34, 35, 38, 39] In this case, vacuum ultraviolet (VUV) radiation at 118 nm (10.5 eV) crosses the molecular beam at right angles and is utilized for photoionization detection of 2-butenal oxide. The VUV radiation is generated by frequency tripling the third harmonic output (~35 mJ pulse^{-1}) of a Nd:YAG laser (Continuum Powerlite 9010, 10 Hz) in a phase matched Xe:Ar gas mixture. The 2-butenal oxide is detected on the parent mass channel (m/z 86).

A broadly tunable β-barium borate optical parametric oscillator (BBO-OPO) source (EKSPLA 342NT, 3-5 ns pulse width, < 5 cm^{-1} linewidth, 5 Hz) provides UV-vis radiation across the 318-500 nm region. The UV-vis radiation is introduced ~50 ns prior to the VUV radiation. The signal output is utilized in the 410-500 nm region and sum frequency generation (SFG) of the signal output + 1064 nm Nd:YAG fundamental is utilized in the 318-409 nm region. The wavelength (vacuum) of the BBO-OPO output is calibrated using a high-resolution wavemeter (Coherent WaveMaster). The UV-vis OPO power is measured with a power meter (Gentec TPM-300). The counter-propagating UV-vis radiation is focused (40 or 60 cm focal length (f.l.) lens for $\lambda > 410$ nm or $\lambda < 410$ nm, respectively) in the interaction region and spatially overlapped with the VUV radiation. The BBO-OPO pump source and VUV probe are operated at 5 Hz and 10 Hz, respectively, to obtain the percentage depletion of the photoionization signal, $[(\mathrm{OPO_{off}} - \mathrm{OPO_{on}})/\mathrm{OPO_{off}} \times 100\%]$, on alternating pulses.

In the second type of the experiment, the O (^{1}D) products released upon UV-vis excitation of 2-butenal oxide are characterized using velocity map imaging (VMI).[24, 27, 40-45] In this case, UV-vis 'pump' radiation in the 342-459 nm range is generated using the frequency-doubled or fundamental output of a dye laser (Radiant Dyes, NarrowScan; LDS 698, LDS 722, LDS751; Stilbene 420; Coumarin 440, 460) pumped by a Nd:YAG laser (InnoLas, SpitLight 600). After a short time delay (~50 ns), the resultant O (^{1}D) products are state-selectively ionized via (2+1) resonance enhanced multiphoton ionization (REMPI) at 205.47 nm (ca. 1 mJ pulse^{-1}), which is scanned over the O-atom Doppler profile (±0.4 cm^{-1}).[46] The REMPI 'probe' radiation is generated by frequency tripling the output of a dye laser (Continuum, ND6000, Rhodamine 610, 0.08 cm^{-1} linewidth) pumped by the second harmonic output of a Nd:YAG laser (Continuum, Powerlite 8010).

Again, the counter-propagating UV-vis pump (50 cm f.l.) and REMPI probe (40 cm f.l.) lasers are focused and spatially overlapped in the interaction region. Both laser polarizations are aligned to be parallel to the detector plane. The ions generated are velocity mapped by a set of three ion optics onto the temporally and spatially sensitive multi-channel plate (MCP) detector coupled with a phosphor screen, which is temporally gated for the O$^+$ mass channel (m/z 16). The central region of the detector is protected by a physical beam block (3 mm diameter), which prevents ions with low translational energy

(≤ 300 cm^{-1}) from striking the MCP plate.[42, 43] The 2D spatial images are collected by a CCD camera and analyzed using the pBASEX inversion method to extract angular and velocity distributions of the O (^{1}D) products,[47] resulting in an energy resolution (ΔE/E) is of ~10%. The UV-vis pump and REMPI probe lasers are operated at 5 Hz and 10 Hz, respectively, to perform background subtraction. Background O (^{1}D) atoms arise from one-color photodissociation of 2-butenal oxide, IO by-products,[48] and possibly other sources, which are ionized by 205 nm radiation.

2.2 Theoretical

In a previous study,[13] ground state geometry optimization and anharmonic frequency calculations were carried out for the eight conformers of 2-butenal oxide using the B2PLYP-D3/cc-pVTZ level of theory as implemented in Gaussian 16.[49] The energies of the eight conformers were then evaluated at the CCSD(T)-F12b/cc-pVTZ-F12 level of theory.[13] The resulting relative energies are given in Figure 1 and Table S1, which are zero-point corrected using anharmonic frequencies from B2PLYP-D3/cc-pVTZ calculations.[13] The B2PLYP-D3/cc-pVTZ level of theory is known to work well for obtaining accurate minimum energy and transition state geometries, as well as associated normal mode wavenumbers, for a number of Criegee intermediates.[23, 45, 50] The geometry optimizations and frequency calculations in this study are performed with this functional and basis set combination unless otherwise stated.

Several isomers of 2-butenal oxide can be formed via unimolecular rearrangements (Scheme S2-S5), and thus are optimized and zero-point energy (ZPE) corrected. The computed adiabatic and vertical ionization energies (AIE and VIE) of the eight conformers of 2-butenal oxide and relevant isomers are summarized in Table S1. The AIE is the minimum amount of energy required to remove an electron from the neutral species combined with the difference in ZPE between the cation and the neutral. The VIE is simply the energy difference between the cation and the neutral with identical nuclear configuration (ground state minimum energy geometry).

Vertical excitation energies (VEE, Table S2) are calculated using the Complete Active Space Second Order Perturbation Theory (CASPT2) coupled to the aug-cc-pVDZ basis set as implemented in MOLPRO v2020.1.[51-53] The CASPT2 calculations are based on a seven-singlet state-averaged Complete Active Space Self-Consistent Field (SA7-CASSCF) reference wavefunction involving an active space of 14 electrons in 12 orbitals (14,12). The occupied orbitals consist of three delocalized π orbitals, one 2p orbital localized on the oxygen atoms, and three σ orbitals involving the carbonyl oxide functional group. The virtual orbitals consist of two delocalized π* orbitals, one σ* orbital localized on the carbonyl oxide moiety, and two diffuse Rydberg orbitals, R(3s) and R(3p). Previous studies on the MVK-oxide and MACR-oxide suggested that the Rydberg R(3s) orbital is essential for accurate evaluation of VEEs.[24, 27] Although (12,10) was shown to be adequate for MVK-oxide and MACR-oxide,[24, 27, 54] the larger (14,12) active space is chosen in this study to ensure consistency of the active space across the eight conformers of 2-butenal oxide. An imaginary level shift of 0.4 Hartree is applied to the CASPT2 calculations to mitigate the involvement of intruder states. Oscillator strengths (f) for the spin-allowed transitions are calculated using the CASSCF transition dipole moments (μ_{ij}) associated with the electronic transition from state i to state j with CASPT2 energies (E_{ij}),

$$f_{ij} = \frac{2}{3} E_{ij} \sum_{\alpha=x,y,z} |\mu_{ij}|_{\alpha}^{2} \tag{1}$$

There are many possible isomers of 2-butenal oxide (m/z 86, Scheme S2-S5), for which we have computed VEEs and oscillator strengths using the same CASPT2(14,12)/aug-cc-pVDZ methods (Table S3). However, we have not identified any plausible isomer with strong electronic transitions in the 300-500 nm region.

UV-vis absorption profiles are then simulated for the four lowest energy conformers of 2-butenal oxide using a nuclear ensemble approach similar to that described for other Criegee intermediates.[50, 54] For each conformer (*cZE*, *tZE*, *tEE*, *tZZ*), an ensemble of 100 initial geometries (N_{TOT}) is sampled using a Wigner distribution based on the RASSCF(14,12)/aug-cc-pVDZ optimized ground state minimum energy geometries and associated normal mode wavenumbers using SHARC 2.1.1.[55-57] Each of the returned geometries is then extracted, and the corresponding VEEs and oscillator strengths are computed using the same CASPT2(14,12)/aug-cc-pVDZ method in MOLPRO v2020.1. An energy-dependent absorption cross-section P(E) for each conformer is determined by summing over the 100 Wigner geometries and the final states of interest (M)

$$P(E) = \frac{\pi e^2}{2 m_e c \varepsilon_0} \sum_{j=1}^{M} \left[\frac{1}{N_{TOT}} \sum_{N=1}^{N_{TOT}} f_{ij}^{N} g(E - \Delta E_{ij}^{N}, \delta) \right] \tag{2}$$

Here m_e and e are the mass and charge of an electron, c is the speed of light, and ε_0 is the vacuum permittivity. A Lorentzian line shape function (g) with a broadening factor $\delta = 0.\ 2$ eV is assumed for each transition, and $\hbar$ is the Planck's constant.

$$g\left(E - \Delta E_{ij}^{N}, \delta\right) = \frac{\hbar \delta}{2\pi} \left(\left(E - \Delta E_{ij}^{N}\right)^2 + \left(\frac{\delta}{2}\right)^2 \right)^{-1} \tag{3}$$

The resultant simulated absorption spectra for the lowest four conformers of 2-butenal oxide are shown in Figure S2. The computed spectra will be described and compared with the experimental results in the Results section.

The unrelaxed potential energy curves for the first seven singlet electronic states of the lowest energy *cZE* conformer of 2-butenal oxide are evaluated along the O-O dissociation coordinate (R_{OO}) using the CASPT2(14,12)/aug-cc-pVDZ level of theory. The full set of utilized orbitals are depicted in Figure S3. This calculation is performed by elongating the O-O distance while keeping the remainder of the nuclear framework fixed at the ground state minimum energy geometry of 2-butenal oxide.

Next, the energy required for the spin-allowed dissociation of the *cZE* conformer of 2-butenal oxide to O (^{1}D) and *cE* conformer of 2-butenal (S_0) products is evaluated using the same multireference method and active space (14,12). A constrained optimization (excluding the COO angle which was fixed at the ground state equilibrium value to facilitate convergence) was carried out for 2-butenal oxide by fixing the O-O bond distance to 4.0 Å and allowing the remainder of the nuclear framework to relax to their respective B2PLYP-D3/cc-pVTZ minima. The resulting relaxed structure was then single-point energy corrected using CASPT2(14,12)/aug-cc-pVDZ. The predicted dissociation energy includes the CASPT2 energy difference between 2-butenal oxide and dissociation products, along with the corresponding anharmonic ZPE difference (B2PLYP-D3/cc-pVTZ). The zero-point corrected dissociation energies for other conformers of 2-butenal oxide are shown in Table S4, considering the relative ground state stabilities (Table S1) of 2-butenal oxide and the corresponding conformational form of the 2-butenal product (anharmonic ZPE corrected B2PLYP-D3/cc-pVTZ energy, Table S4).

The Gaussian and MOLPRO calculations were performed utilizing XSEDE resources.[58]

3. Results

3.1 Electronic spectroscopy of 2-butenal oxide

This study examines the electronic spectroscopy and photodissociation dynamics of the 2-butenal oxide Criegee intermediate following excitation of the strongly absorbing $\pi^* \leftarrow \pi$ electronic transitions, and compares the results to analogous studies undertaken on the four-carbon Criegee intermediates derived from isoprene ozonolysis (MVK-oxide and MACR-oxide). The 2-butenal oxide Criegee intermediate is detected via VUV photoionization at 10.5 eV using TOF-MS. The 10.5 eV photoionization energy is sufficient to ionize the eight conformers of 2-butenal oxide based on their calculated vertical ionization energies that range between 8.2-8.7 eV (Table S1).

CASPT2 calculations indicate that the lowest electronically excited state (S_1) of 2-butenal oxide has $n\pi^*$ character with negligible oscillator strength, as found for other Criegee intermediates.[14, 24, 27, 45, 59] By contrast, excitation to the S_2 and S_3 states involves strong $\pi^* \leftarrow \pi$ transitions as indicated in Table 1. The VEEs to the first $^1\pi\pi^*$ states of the eight conformers of 2-butenal oxide are computed at 3.1-3.6 eV, corresponding to a wide span of 400-350 nm with significant oscillator strengths ranging from 0.07 for *cZE* to 0.15 for *tEE*. The range of VEEs predicted for 2-butenal oxide conformers is comparable to those for MVK-oxide (3.2-3.5 eV) and MACR-oxide (3.3-3.6 eV), but notably shifted to lower energy (longer wavelength) than CH_2OO and alkyl-substituted Criegee intermediates due to extended conjugation across the vinyl and carbonyl oxide groups.[15, 24, 27, 34, 35, 38] The VEEs for the second $\pi^* \leftarrow \pi$ transition of 2-butenal oxide are predicted at 4.2-4.7 eV, corresponding to 300-270 nm and have slightly weaker oscillator strengths in the range of 0.04-0.09. This second $^1\pi\pi^*$ state will be experimentally explored in future studies. Additional electronically excited states of 2-butenal oxide with nπ* (S_4), π3s (S_5), and n3s (S_6) character are predicted at higher energies (Table S2) beyond the near-UV region with much weaker oscillator strengths, and are not the focus of this study.

Table 1. Vertical excitation energies (VEE, eV), corresponding wavelengths (λ, nm) and the oscillator strengths (*f*) computed at the CASPT2(14,12)/aug-cc-pVDZ level of theory for electronic transitions of the eight conformers of 2-butenal oxide to the first and second ${}^1\pi\pi^*$ states.

Conformer							
cZE		*tZE*		*tEE*		*tZZ*	
VEE / eV (λ / nm)	*f*	VEE / eV (λ / nm)	*f*	VEE / eV (λ / nm)	*f*	VEE / eV (λ / nm)	*f*
3.47 (357)	0.072	3.11 (398)	0.099	3.32 (374)	0.146	3.16 (392)	0.095
4.62 (268)	0.042	4.68 (265)	0.085	4.22 (294)	0.058	4.67 (266)	0.062
tEZ		*cEE*		*cEZ*		*cZZ*	
VEE / eV (λ / nm)	*f*	VEE / eV (λ / nm)	*f*	VEE / eV (λ / nm)	*f*	VEE / eV (λ / nm)	*f*
3.35 (371)	0.139	3.09 (401)	0.117	3.15 (393)	0.109	3.57 (348)	0.070
4.24 (293)	0.073	4.28 (290)	0.070	4.15 (298)	0.082	4.54 (278)	0.042

Experimentally, UV-vis excitation resonant on the first π*←π transition of 2-butenal oxide readily depletes the ground state population of one or more of the conformers. The ground state depletion is detected after a short time delay (Δt ~50 ns) as a reduced VUV photoionization signal on m/z 86. The inset of Figure 2 shows a representative ground state depletion in which excitation at 410 nm induces a significant decrease in the VUV photoionization signal at m/z 86. The percentage depletion at 410 nm increases with OPO power to ca. 40% depletion at 10 mJ pulse^{-1}. A minimum reliable depletion of 3% is required at current signal level. The magnitude of the depletion can be expressed as $[(N_0-N)/N_0 \times 100\%]$ where N and N_0 represent ground state abundances with and without excitation. The corresponding absorbance, $[-\ln(N/N_0)]$, scales linearly with OPO power at 410 nm, as shown in Figure 2, indicative of a one-photon absorption process. A separate linear UV power dependence is also obtained at 340 nm (Figure S4).

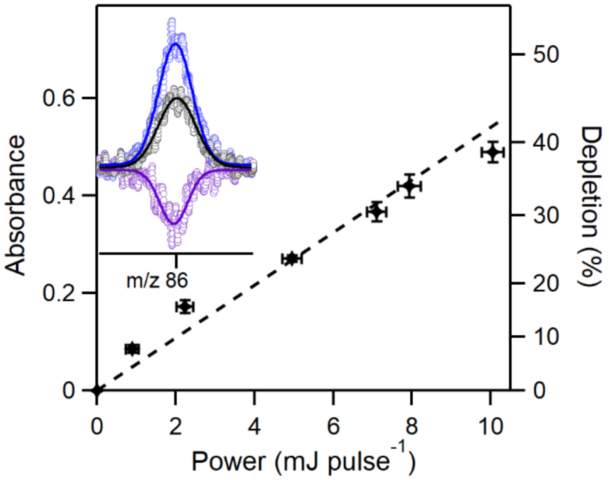

Figure 2. Percentage depletion of the m/z 86 (2-butenal oxide$^+$) photoionization signal as a function of OPO power at 410 nm. The absorbance shows a linear dependence (dashed line) with OPO power, indicating a one-photon process. The error bars on both axes represent the standard deviations (±1σ) derived from repeated measurements. The blue trace of the inset shows the 2-butenal oxide mass spectrum (m/z 86) arising from VUV photoionization at 118 nm (10.5 eV). The black trace shows a reduced (~40%) photoionization signal upon excitation at 410 nm (10 mJ pulse^{-1}), which is induced by a ground state depletion. The purple trace shows the depletion signal ($OPO_{on} - OPO_{off}$).

Potential isomers that may be formed (Scheme S2-S5) and ionized by the 10.5 eV VUV radiation are not predicted to have electronic transitions with strong oscillator strengths in the 300-500 nm range (Table S1 and S3), and thus will not contribute to the depletion signal. Nevertheless, photoionization signals from isomers will contribute to the population in the denominator, N_0, and limit the maximum apparent depletion that is measured.

The electronic spectrum of 2-butenal oxide shown in Figure 3 is recorded in 1 nm steps in the UV-vis range of 318-500 nm. The OPO power is maintained at ca. 2 mJ pulse^{-1} in the SFG output region ($\lambda <$ 410 nm) and ca. 7 mJ pulse^{-1} in the signal output region ($\lambda \geq$ 410 nm). In both spectral regions, linear power dependence is verified and the averaged data points from repeated measurements (typically ~4000 OPO pulses) are normalized by power. The gray shading accounts for the ±1σ uncertainty in the measurements. The experimental spectrum is broad and asymmetric in shape with a primary peak at 373 nm and a secondary peak at 342 nm. On the longer wavelength side, the spectrum drops to half maximum at ca. 420 nm. By contrast, a more rapid decline on the short wavelength side drops to half maximum at ca. 320 nm.

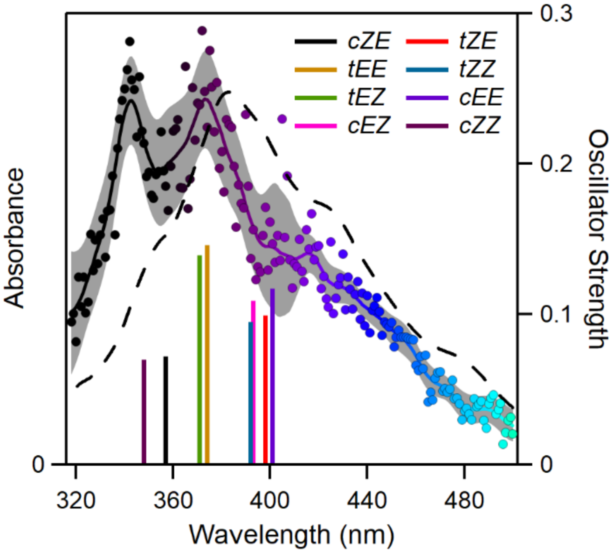

Figure 3. Experimental UV-vis spectra of 2-butenal oxide from 318 to 500 nm derived from depletion of the photoionization signal on the m/z 86 mass channel. The corresponding absorbance (points) is normalized by OPO power. The solid line is a smoothed curve (9 points) through the experimental data point with ±1σ uncertainty indicated by the gray shaded region. The black dashed line is the simulated absorption spectrum of *cZE* conformer of 2-butenal oxide for the first π*←π transition. The computed CASPT2(14,12)/aug-cc-pVDZ VEEs and associated oscillator strengths (bars) are shown for promotion of 2-butenal oxide to the $1^1\pi\pi^*$ state for the eight conformers.

For comparison, the electronic spectra of 2-butenal oxide originating from the ground state of the four lowest energy conformers were theoretically computed using the nuclear ensemble method. The simulated electronic absorption profile for the lowest energy *cZE* conformer is shown in Figure 3 (and Figure S2), while those from the higher energy conformers (*tZE*, *tEE* and *tZZ*) are shown in Figure S2. The simulated absorption profiles indicate that the experimental spectrum across the 318-500 nm region predominantly originates from the first π*←π electronic transitions of 2-butenal oxide. The predicted first absorption profiles are broad with full-width at half-maximum (FWHM) of ca. 100 nm for *cZE, tZE* and *tEE*, and ca. 130 nm for *tZZ*, which are comparable to the 100 nm breadth (FWHM) of the experimental spectrum. The breadth of the simulated absorption bands for each conformer reflects the Franck-Condon profiles associated with the 100 initial ground state geometries sampled.

The absorption maximum of the simulated first π*←π band is predicted at 382 nm for the lowest energy *cZE* conformer and is in good accord with the experimental absorption spectrum, especially near the primary peak of 373 nm and at longer wavelengths. The absorption maxima predicted for other conformers are shifted to slightly longer wavelengths of 419 nm (*tZE*), 398 nm (*tEE*), and 398 nm (*tZZ*). The spectral peak absorption for each conformer is predicted at longer wavelength (lower energy) than the corresponding VEE from the ground state minimum energy geometry by 0.05-0.22 eV. This phenomenon is commonly observed with the nuclear ensemble method due to the frequency changes between the ground and excited states and, as a result, the simulated spectra provide a better comparison with the experimental spectra.[60] The resultant peak absorption cross-sections from spectral simulations (Table 2) are on the order of 10^{-18}-10^{-17} cm^2, as found for prototypical Criegee intermediates studied previously.[14] The intensity trend of absorption cross-sections is consistent with that for oscillator strengths from the ground state minimum geometries (Table 1).

Table 2. Calculated photoabsorption cross-sections (σ) of four conformers of 2-butenal oxide, at the peak of the first $\pi^*\leftarrow\pi$ transition band.

Conformer	σ ($\times 10^{-17}$ cm^2)
cZE	0.46
tZE	0.94
tEE	1.22
tZZ	0.84

The contribution of higher energy conformers of 2-butenal oxide to the experimental absorption spectrum is not known. Among the lowest four conformers of 2-butenal oxide, *cZE* (0 kcal mol^{-1}) is expected to have the highest population but has the smallest absorption cross-section. On the other hand, the *tEE* conformer (1.5 kcal mol^{-1}) may be less populated but is predicted to have the largest absorption cross-section. As a result, either the *tEE* conformer or others could lead to the secondary peak at 342 nm observed experimentally.

Finally, the simulated electronic absorption spectra for the second $\pi^*\leftarrow\pi$ transitions of the various conformers of 2-butenal oxide are predicted to peak at much shorter wavelengths. Some overlap between the two $\pi^*\leftarrow\pi$ transitions is predicted for *cZE* and *tEE* conformers at $\lambda < 340$ nm. Nevertheless, a rapid fall-off in the experimental absorption spectrum is observed at $\lambda < 342$ nm, and thus we assume that the second $\pi^*\leftarrow\pi$ absorption band is less relevant to the present study.

3.2 Photodissociation dynamics of electronically excited 2-butenal oxide

The photodissociation dynamics of the 2-butenal oxide Criegee intermediate upon UV-vis excitation corresponding to the first $\pi^*\leftarrow\pi$ transition has been investigated using a combined experimental and theoretical approach. Starting with theory, the potential energy curves (unrelaxed) for the first seven singlet electronic states of the lowest energy *cZE* conformer of 2-butenal oxide are evaluated along the O-O dissociation coordinate (R_{OO}) using the CASPT2(14,12)/aug-cc-pVDZ level of theory. The resultant adiabatic potential energy curves are shown in Figure 4. Vertical excitation is predicted to access the regions of the excited S_2 ($^1\pi\pi^*$) state potential energy surface that is repulsive with respect to increasing R_{OO}. Along R_{OO}, this state shows an avoided crossing (at ca. R_{OO} ~1.7 Å) with electronic states that are also repulsive with respect to O-O bond elongation, leading to the lowest spin-allowed dissociation asymptote of O (^{1}D) + 2-butenal (S_0). The lowest spin-allowed dissociation asymptote is computed at 2.18 eV (568 nm, 17600 cm^{-1}) for the *cZE* conformer, which is far lower than the UV-vis excitation energies, suggesting exoergic O-O bond fission following ππ* excitation. Dissociation energies are predicted for other conformers by considering the relative stabilities of the 2-butenal oxide Criegee intermediate and its corresponding 2-butenal product (Table S4). Similar dissociation pathways have been computed for other Criegee intermediates, including CH_2OO, MVK-oxide, and MACR-oxide.[24, 27, 59]

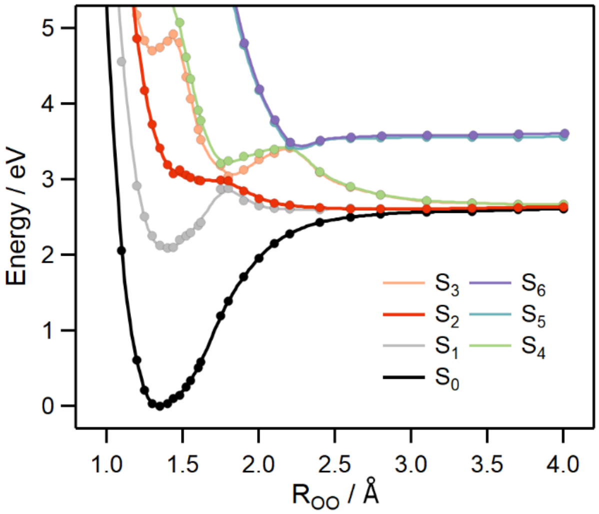

Figure 4. Adiabatic potential energy curves (unrelaxed) computed along the O-O bond dissociation coordinate (R_{OO}) for the lowest seven singlet states of the *cZE* conformer of 2-butenal oxide. The lower five states lead to the O (^{1}D) + 2-butenal (S_0) product asymptote, while the higher two states lead to the O (^{3}P) + 2-butenal (T_1) product asymptote. Calculations are conducted at CASPT2(14,12)/aug-cc-pVDZ level of theory.

Experimentally, the photodissociation dynamics of 2-butenal oxide is probed using velocity map imaging, which involves 2+1 REMPI detection of O (^{1}D) products to obtain radial and angular distributions of the O (^{1}D) products, following excitation at wavelengths in the range 342-459 nm, covering the experimentally measured electronic absorption spectrum. Representative VMI images obtained at 357, 420, and 459 nm are displayed in Figure 5; additional images are provided in Figure S5. The UV-vis laser-induced O (^{1}D) REMPI signal follows the absorption spectrum (Figure 3), falling off beyond 480 nm.

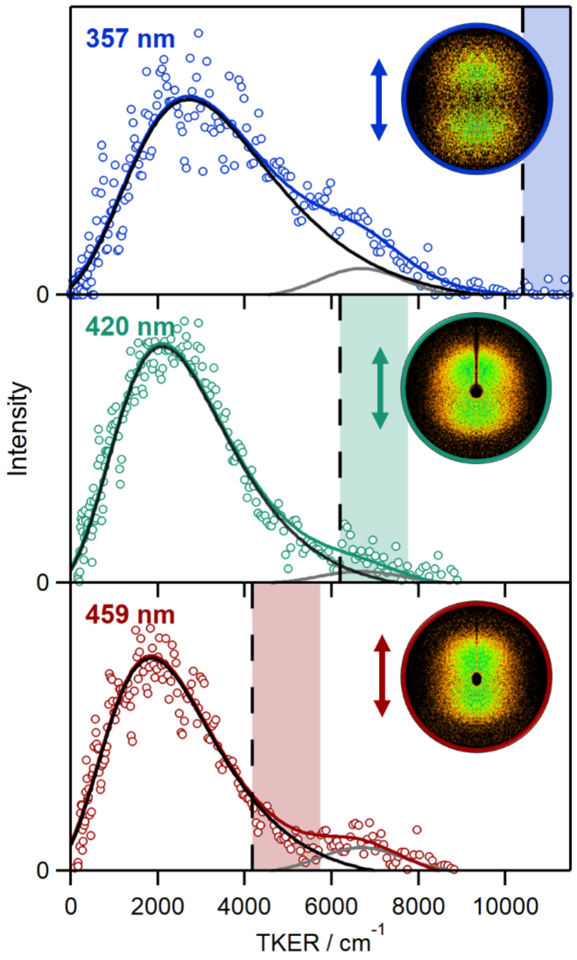

Figure 5. Total kinetic energy release (TKER) distributions (open circles) and the fits (colored lines) obtained by velocity map imaging of O (^{1}D) products following UV-vis excitation at 357 nm (upper), 420 nm (middle), and 459 nm (lower). In each panel, a weak IO component (gray curves) arising from incomplete background subtraction is fit with Gaussian distribution centered at 6680 cm^{-1}. The TKER distributions for the O (^{1}D) + 2-butenal (S_0) product channel are well represented by Gumbel distributions (black lines). The vertical black dashed lines indicate the energy available (E_{avl}) to products for the *cZE* conformer of 2-butenal oxide at each UV-vis wavelength with the shaded region indicating E_{avl} for less stable conformers. Insets are the corresponding raw images of the O (^{1}D) photoproducts. The double-sided arrows represent the polarization of the UV-vis radiation.

The angular distributions of O (^{1}D) products are anisotropic (Table S5), indicating rapid dissociation that is faster than the rotational period (ca. 100 ps) of 2-butenal oxide[61] and suggesting a high yield for dissociation. Integration over the angular distribution of the VMI image yields the radial distribution, which in turn provides the velocity distribution of the O (^{1}D) product. The total kinetic energy release (TKER) distribution is then derived using conservation of linear momentum.

The resultant TKER distributions shown in Figure 5 (and Figure S5) are broad and unstructured, but include a small background component in the 5000-8000 cm^{-1} range. The latter is due to incomplete background subtraction of O (^{1}D) products arising from one-color photodissociation of IO and 2+1 ionization of the resultant O (^{1}D) products at 205 nm.[43, 44] This background component is removed using a Gaussian distribution peaked at 6680 cm^{-1}, arising from the well-known bond dissociation energy of IO,[48] with breadth of 2300 cm^{-1}. This IO background signal accounts for less than 10% of the total TKER distribution by area. Additional detail is provided in Section SC and Figure S6. The TKER distributions arising from 2-butanal oxide are then fit with a Gumbel distribution (Table S6), as in prior studies,[39, 45] yielding the average TKER (⟨TKER⟩) and FWHM (Table 3 and Table S5).

The energy available (E_{avl}) to products at each excitation wavelength is evaluated using conservation of energy, $E_{avl} = h\nu - D$, where $h\nu$ is the photon energy and D is the energy required for dissociation of the *cZE* conformer of 2-butenal oxide to O (^{1}D) + 2-butenal (S_0) products. The internal energy of 2-butenal oxide is assumed to be negligible under jet-cooled conditions. Hence, E_{avl} increases from 4200 to 11600 cm^{-1}, indicated by the dashed vertical lines in Figure 5, as the UV-vis excitation energy increases from 21800 to 29200 cm^{-1} (459 to 342 nm). Higher energy conformers of 2-butenal oxide, to the extent populated, may release as much as 1600 cm^{-1} of additional energy to products (Table S4) as shown by the shaded regions in Figure 5.

Table 3. Properties of the total kinetic energy release (TKER) distributions derived from velocity map imaging of O (^{1}D) products following UV-vis excitation of 2-butenal oxide.

λ (nm)	E_{avl}[a] (cm^{-1})	Peak (cm^{-1})	⟨TKER⟩ (cm^{-1})	FWHM (cm^{-1})	E_{int} (cm^{-1})	$\frac{E_{int}}{E_{avl}}$ (%)	IO (%)
342	11620	2920	4130	5240	7490	64	6
357	10400	2710	3670	4130	6730	65	7
380	8700	2490	3360	3780	5340	61	5
420	6190	2100	2860	3270	3330	54	3
437	5270	2280	3140	3730	2130	40	0
447	4760	1950	2710	3300	2050	43	3
459	4170	1850	2580	3180	1590	38	8

[a] Estimated from UV-vis excitation energy and zero-point energy corrected dissociation energy for the lowest energy *cZE* conformer of 2-butenal oxide (see Table S4). Higher energy conformers have lower dissociation energies and thus greater E_{avl}.

The available energy can be partitioned into kinetic energy of the fragments (TKER) and internal energy (E_{int}) of the 2-butenal products as $E_{avl} = \text{TKER} + E_{int}$. As shown in Figure 5, the TKER distributions extend to E_{avl}, consistent with the theoretically predicted dissociation energy. As the photon and corresponding available energy increases, the average TKER increases from 2600 to 4100 cm^{-1} and the TKER distributions broaden (3200 to 5200 cm^{-1} FWHM). The percentage of E_{avl} flowing into E_{int}

increases from 38% to 64%, corresponding to a higher degree of internal excitation of 2-butenal products, with increasing excitation of the Criegee intermediate.

3.3 Reduced impulsive model for photodissociation dynamics

A reduced impulsive model is utilized to simulate the kinetic energy release associated with dissociation of electronically excited 2-butenal oxide to O (^{1}D) + 2-butenal (S_0) products and compared with the experimental TKER distribution. The model is illustrated using the lowest energy *cZE* conformer of 2-butenal oxide and the corresponding *cE* conformer of the 2-butenal product. In this model, the available energy (h*ν*-D) is released as translational energy of the recoiling fragments and vibrational excitation of the 2-butenal product. The torque imparted on the 2-butenal product by the leaving O-atom is expected to primarily result in bending motions involving $HC_{(1)}O$ or $OC_{(1)}C_{(2)}$ angles. The O-O bond fission is unlikely to impart significant rotational excitation to the heavy 2-butenal partner and thus rotational excitation of 2-butenal is neglected.

The simple vibrational reflection principle[62] predicts a high degree of vibrational excitation in the product along vibrational coordinates with equilibrium values significantly different from the parent molecule. Therefore, the geometric changes from 2-butenal oxide to 2-butenal are evaluated to reveal the vibrational modes that are likely to be excited (Figure S7). Substantial geometric changes (Table S7) are identified in the vicinity of the carbonyl group, especially a -0.07 Å compression in the C=O bond length and +9.3° expansion in the $HC_{(1)}O$ angle. As a result, we anticipate that $C_{(1)}C_{(2)}$ stretch, $C_{(1)}H$ stretch, CO stretch, $C_{(1)}H$ in-plane wag, $OC_{(1)}C_{(2)}$ bend, and $C_{(2)}C_{(3)}C_{(4)}$ bend vibrations (Figure S8) will be excited in the 2-butenal product. Since both 2-butenal oxide and 2-butenal are planar, we do not expect excitation of out-of-plane vibrations. This is consistent with the lack of out-of-plane forces during O-O bond cleavage in prior trajectory calculations of CH_2OO and CH_3CHOO photodissociation.[63]

The reduced impulsive model assumes that all energetically allowed vibrational states involving the six selected vibrational modes (assuming harmonic frequencies) are populated equally. The density of translational states is expressed as $\rho(E_T) = A_T(E_{avl} - E_{vib})^{1/2}$, where E_T is the translational energy constrained by conservation of energy ($E_T = E_{avl} - E_{vib}$) and A_T is a normalization factor. The simulated translational energy distribution is then obtained by summing over all vibrational states and taking the experimental resolution of the VMI apparatus ($\Delta E/E \sim 10\%$) into account utilizing a Lorentzian line shape.

Simulated translational energy distributions are compared with the experimental TKER distributions obtained upon excitation of 2-butenal oxide at 357, 420, and 459 nm in Figure 6 and at additional wavelengths in Figure S9. Good agreement is obtained between the simulated translational energy distributions and experimental TKER distributions across a wide range of UV-vis excitations (342-459 nm) and corresponding available energies (E_{avl} = 11600-4200 cm^{-1}). The simple reduced impulsive model provides a good representation of both the most probable kinetic energy and the breadth (FWHM) of the TKER distribution. Several additional factors may affect the TKER simulations, including more accurate determination of their dissociation energies, along with vibrational anharmonicity and possible rotational excitation of products.

Simulations of the TKER distributions for other conformers of 2-butenal oxide are obtained using the same impulsive model, taking into account their ground state stabilities, dissociation energies, and the vibrational frequencies of their respective 2-butenal products. The dissociation energies alone change by as much as 1600 cm^{-1} for different conformers of 2-butenal oxide. Simulations of the TKER distributions are repeated for several conformers, specifically *tZE*, *tEE,* and *tZZ* (Figure S10), but very little change is observed in the derived kinetic energy distributions.

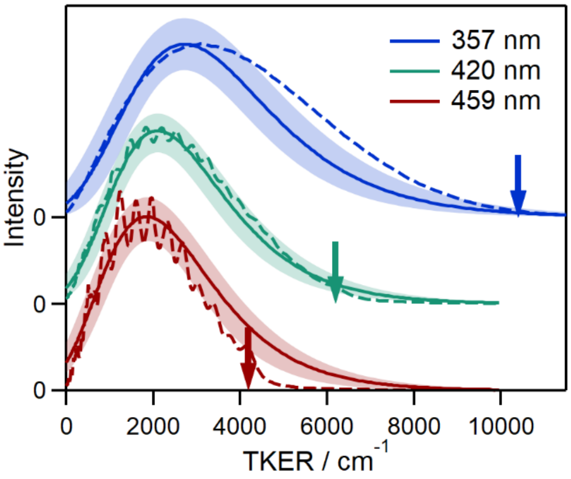

Figure 6. Simulated translational energy distributions for the O (^{1}D) + 2-butenal products using the reduced impulsive model (dashed line) with the best fit to the experimental TKER distributions (solid line) obtained upon electronic excitation of 2-butenal oxide at 357 nm (blue), 420 nm (green) and 459 nm (maroon). The shaded region denotes the standard deviation (±1σ) of each fit to the experimental data.

4. Discussion

4.1 Electronic spectroscopy

In this section, the properties of the 2-butenal oxide Criegee intermediate are compared with those for its isoprene-derived isomers of MVK-oxide and MACR-oxide. All three isomers are four-carbon, unsaturated Criegee intermediates with extended conjugation across the carbonyl oxide and vinyl groups, differing by the location of the methyl substituent (Scheme 1). This permits direct theoretical comparison of their ground state stabilities, along with the stabilities of the 2-butenal, MVK, and MACR isomeric products (Figure S11). Specifically, this comparison shows that the most s conformer of MVK-oxide (*syn-trans*) is 3.6 kcal mol^{-1} more stable in absolute energy than the most stable conformer of 2-butenal oxide (*cZE*), which in turn is 2.3 kcal mol^{-1} more stable in absolute energy than the most stable conformer of MACR-oxide (*anti-trans*).[23, 24]

Two strong π*←π transitions have been predicted for MVK-oxide and MACR-oxide,[24, 27] and analogous transitions are computed for the 2-butenal oxide Criegee intermediate (Table 1). Here, we compare the experimental spectrum of 2-butenal oxide with those for its isoprene derived isomers in the 300-500 nm region associated with promotion to the first $^1\pi\pi^*$ state ($S_2 \leftarrow S_0$). The experimental spectrum for jet-cooled 2-butenal oxide is overlaid on previously reported spectra for MVK-oxide and MACR-oxide collected under similar conditions with normalized peak absorption in Figure 7.[24, 27, 39]

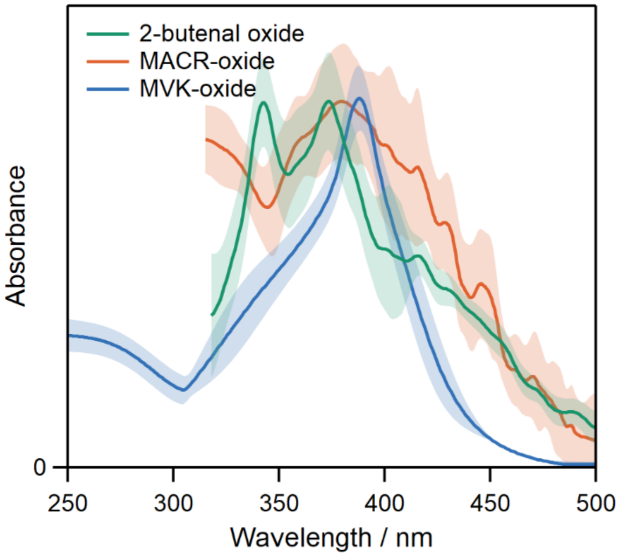

Figure 7. Comparison of smoothed UV-vis absorption spectra obtained for 2-butenal oxide (green), MACR-oxide (orange), and MVK-oxide (blue) under jet-cooled conditions, displayed with normalized peak absorption and shaded regions indicating uncertainty (±1σ based on repeated measurements). The absorption spectrum of MACR-oxide is reproduced with permission from Ref. 24, Copyright 2019 J. Am. Chem. Soc. The absorption spectrum of MVK-oxide is reproduced with permission from Ref. 39, Copyright 2021 J. Chem. Phys.

The primary absorption peak of 2-butenal oxide (373 nm) is similar to those reported previously for MVK-oxide (388 nm) and MACR-oxide (380 nm). In each case, extended conjugation in these systems shifts the peak absorption to significantly longer wavelength than found for CH_2OO (ca. 335 nm) and alkyl-substituted Criegee intermediates under analogous experimental conditions [e.g. $(CH_3)_2COO$ at ~320 nm].[15, 24, 27, 34, 35, 38] In the visible region, the 2-butenal oxide and MACR-oxide spectra are similar to one another with slowly decreasing absorption extending to 500 nm, although MACR-oxide exhibits weak oscillatory structure superimposed on its broad profile.[24] In contrast, MVK-oxide exhibits a rapid drop off in absorption from 400 to 450 nm.[27] On the shorter wavelength side (λ < 370 nm), 2-butenal oxide exhibits a secondary peak at ca. 340 nm, likely due to overlapping contributions from multiple conformers, and then falls off rapidly to 320 nm. The second π*←π transition for 2-butenal oxide is predicted at shorter wavelength than explored in this study. (Table 1) The absorption band associated with the second π*←π transition of MVK-oxide is evident below ca. 300 nm;[39] the onset of the second π*←π transition of MACR-oxide may occur below 340 nm, but further investigation at shorter wavelength is needed.[24]

Comparison of the computed oscillator strengths (*f*) upon vertical excitation of the lowest energy conformers of 2-butenal oxide (*cZE*, 0.072), MVK-oxide (*syn-trans*, 0.147), and MACR-oxide (*anti-trans*, 0.116) shows that the first π*←π transition of MVK-oxide is predicted to be 20% stronger than that for MACR-oxide and almost 2-fold greater than that for 2-butenal oxide.[24, 27] In addition, comparisons can be made across the three isomers based on the computed absorption cross sections (σ) derived from spectral simulations employing a nuclei ensemble method by sampling ground state geometries with a Wigner distribution.[54] Again, comparing the most stable conformers of each Criegee intermediate, the resultant cross-sections reveal the strongest absorption for *syn-trans* MVK-oxide (1.30×10^{-17} cm^2), somewhat weaker absorption for *anti-trans*-MACR-oxide (1.19×10^{-17} cm^2),[54] and 3-fold weaker absorption for the *cZE* conformer of 2-butenal oxide (0.46×10^{-17} cm^2). The recently reported peak absorption cross sections measured for thermally populated distributions of MVK-oxide [$(3.70 \pm 0.74) \times 10^{-17}$ cm^2] and MACR-oxide [$(3.04 \pm 0.58) \times 10^{-17}$ cm^2] conformers show a similar enhancement in absorption for MVK-oxide compared to MACR-oxide.[64]

4.2 Photodissociation dynamics

Electronic excitation on the first π*←π transitions of 2-butenal oxide, MVK-oxide and MACR-oxide results in prompt O-O bond fission, leading to the lowest spin-allowed product channels of O (^{1}D) + carbonyl (S_0) co-products, specifically 2-butenal, MVK, and MACR products. The dissociation energies computed for the 2-butenal oxide conformers can be compared with those previously reported for MVK-oxide and MACR-oxide (Figure S11).[24, 27] Considering the lowest energy conformers only, the dissociation energy for the *syn-trans* conformer of MVK-oxide (51.9 kcal mol^{-1}) is greater than that for the *cZE* conformer of 2-butenal oxide (50.4 kcal mol^{-1}), which in turn is greater than that for the *anti-trans* conformer of MACR-oxide (47.4 kcal mol^{-1}). More generally, slightly more energy (2-3 kcal mol^{-1}) is required for dissociation of most conformers of MVK-oxide to MVK + O (^{1}D) products (49.2 to 51.9 kcal mol^{-1}) than those for 2-butenal oxide to 2-butenal + O (^{1}D) products (45.8 to 50.4 kcal mol^{-1}) or MACR-oxide to MACR + O (^{1}D) (44.9 to 49.8 kcal mol^{-1}), indicating only a weak dependence on the position of the methyl substituent (Scheme 1).

Next, we compare the TKER distributions derived from VMI studies of the three systems upon UV-vis excitation. Prior VMI studies of MVK-oxide were conducted over the 234 to 420 nm range and those for MACR-oxide were carried out from 385 to 471 nm.[24, 27, 39] In order to make comparisons across the three systems, we group together TKER data obtained with similar energies available to products (E_{avl}) (Figure S12 and Table S8, Groups 1-4). A representative comparison is shown in Figure 8, where the experimental TKER distribution obtained upon photodissociation of 2-butenal oxide at 420 nm is compared with those for MACR-oxide at 430 nm and MVK-oxide at 410 nm, which release similar energies to O (^{1}D) + co-products (S_0) of 6200-6500 cm^{-1} (Group 2). As evident in Figure 8, the TKER distributions for 2-butenal oxide and MACR-oxide are remarkably similar in average TKER (⟨TKER⟩) and breadth (FWHM), while the distribution for MVK-oxide has a 20% lower average TKER and 40% narrower breadth. Analogous changes are evident in ⟨TKER⟩ and FWHM for MVK-oxide compared to 2-butenal oxide or MACR-oxide with other E_{avl} (Figures S12, Table S8). The distinct TKER distribution for MVK-oxide compared to those for 2-butenal oxide or MACR-oxide reflects the different degree of vibrational excitation in the carbonyl co-product upon photodissociation. This can be traced to geometric changes between the carbonyl oxide and carbonyl product using the reduced impulsive model.

Here, we apply the reduced impulsive model to predict the TKER distributions arising from the lowest energy conformers of MACR-oxide (*anti-trans*) and MVK-oxide (*syn-trans*) with the associated carbonyl co-products (*trans*-MACR and *trans*-MVK) released with O (^{1}D), following the same approach used for 2-butenal oxide (*cZE*) to 2-butenal (*cE*) above. In brief, dissociation of each Criegee intermediate results in a significantly shortened C=O bond length, leading to vibrational excitation of the CO stretching mode in the carbonyl products.[23, 24, 39, 65] In addition, the extended π system reduces from five atoms to four atoms, affecting the angles and bond lengths of the carbon backbone and resulting in activation of $C_{(2)}C_{(3)}C_{(4)}$ bend (2-butenal oxide and MACR-oxide) or $C_{(1)}C_{(2)}C_{(3)}C_{(4)}$ ring-closure (MVK-oxide) mode in the carbonyl products with similar frequencies across the three systems. Geometric changes are also predicted in bond lengths and angles involving the H- (2-butenal oxide and MACR-oxide) or methyl- (MVK-oxide) substituent adjacent to the carbonyl oxide group. As a result, $C_{(1)}H$ stretch, $C_{(1)}C_{(2)}$ stretch, $OC_{(1)}H$ bend, and $OC_{(1)}C_{(2)}$ bend are activated in both 2-butenal and MACR products, and these normal modes are similar in frequency for the two aldehyde products. The analogous modes activated in the MVK products are $C_{(1)}C_{(2)}$ stretch, $C_{(1)}C_{(4)}$ stretch, $OC_{(1)}C_{(2)}$ bend, and $OC_{(1)}C_{(4)}$ bend (Tables S7 and S9). However, the methyl substituent of MVK is 15 times heavier than the H-atom substituent of the aldehydes, and the corresponding modes of the ketone are reduced in frequency.[23]

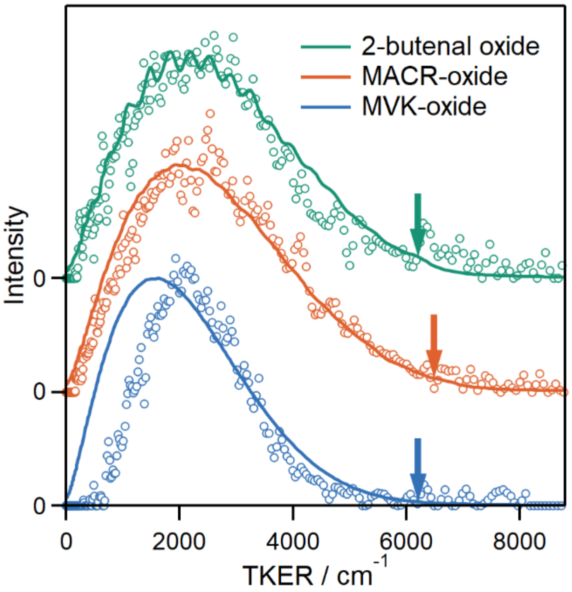

Figure 8. Comparison of experimental TKER distributions (open circles) obtained upon photodissociation of 2-butenal oxide at 420 nm (green), MACR-oxide at 430 nm (orange), and MVK-oxide at 410 nm (blue), which release similar energies (E_{avl}, Table S8) to O (^{1}D) + co-products (S_0) of ca. 6200-6500 cm^{-1} (arrows). Reduced impulsive model simulations (solid lines) are shown for the lowest energy conformer of each Criegee intermediate. The notably lower and narrower TKER distribution for MVK-oxide is indicative of greater vibrational activation of the MVK product compared to the other isomeric systems.

The most important distinction among the three isomeric Criegee intermediates is the weak intramolecular interaction between two H-atoms of the methyl substituent and the terminal oxygen in MVK-oxide (*syn-trans*), which results in a ca. 60° rotation of the methyl group compared to its orientation in MVK as illustrated by the Newman projections along the $C_{(1)}C_{(4)}$ bond in Figure S7 and dihedral angle change in Table S7. Upon photodissociation of MVK-oxide, there will be significant hindered rotational excitation of the methyl group and vibrational activation of the methyl in-plane rock.[24, 39, 66] The density of states is evaluated using Multiwell 2019.[67]

These geometric changes associated with photodissociation of MVK-oxide (*syn-trans*) result in activation of low frequency vibrational modes and hindered methyl rotation in the MVK product. This results in greater internal excitation of the MVK product, which in turn leads to a narrower and lower energy TKER distribution upon photodissociation of MVK-oxide than the other systems. The reduced impulsive model predicts even more highly internally excited MVK products than seen experimentally at low TKER. This suggests the possibility of additional constraints not considered in the simple impulsive model utilized in this work. Nevertheless, the reduced impulsive model captures the main properties of the TKER distributions resulting from photodissociation of four-carbon Criegee intermediates with extended conjugation across the carbonyl and vinyl groups.

5. Conclusions

2-butenal oxide ($CH_3CH=CHCHOO$), a four-carbon Criegee intermediate with extended conjugation across the carbonyl oxide and vinyl groups, has been characterized by electronic spectroscopy on its first $\pi^*\leftarrow\pi$ transition from 320 to 500 nm and the resultant spin-allowed dissociation dynamics to O (^{1}D) + 2-butenal products. The electronic spectrum of jet-cooled 2-butenal oxide has been recorded by UV-vis induced depletion of the associated VUV (10.5 eV) photoionization signal at m/z 86. The broad UV-visible spectrum, attributed to one or more of its eight conformational forms, has its primary peak at ca. 375 nm (ca. 100 nm FWHM) in a linear absorption process. The electronic spectrum of 2-butenal oxide resembles those for isomeric methyl vinyl ketone oxide (MVK-oxide) and methacrolein oxide (MACR-oxide) Criegee intermediates derived from isoprene ozonolysis.[24, 27] In each case, the electronic spectrum extends into the visible region and is shifted to considerably longer wavelength (ca. 50 nm) than CH_2OO or alkyl-substituted Criegee intermediates.[15, 34, 35, 38]

Complementary theoretical calculations predict the vertical excitation energies and associated oscillator strengths for the first $\pi^*\leftarrow\pi$ electronic transition of the 2-butenal oxide conformers from 348 to 401 nm. Associated absorption profiles with peak cross sections on the order of 10^{-17} cm^2 are computed for the lowest energy conformers of 2-butenal oxide based on a Wigner distribution of ground state configurations. The computed spectral properties are in good accord with the observed spectrum for 2-butenal oxide. The energy required for spin-allowed dissociation to 2-butenal + O (^{1}D) products is also evaluated for each 2-butenal oxide conformer based on a constrained optimization at large O-O distance.

Electronic excitation of 2-butenal oxide to the S_2 ($^1\pi\pi^*$) state results in nonadiabatic coupling and rapid dissociation to O (^{1}D) + 2-butenal products, which is observed as anisotropic velocity map images of O (^{1}D) products detected by 2+1 REMPI. The total kinetic energy release (TKER) distributions, derived from the radial distribution of the images upon excitation at fixed wavelengths across the UV-vis spectrum, are broad, unstructured, and extend over the full range of energy available to products based on computed dissociation energies. On average, internal excitation of the 2-butenal product accounts for 38 to 64% of the available energy.

The large degree of internal excitation of the 2-butenal product is associated with the geometric coordinates and corresponding vibrational modes that change significantly upon dissociation, for example, the shortened $C_{(1)}=O$ bond length of the carbonyl product compared to the zwitterionic Criegee intermediate. Simulations of TKER distributions based on a reduced impulsive model that accounts for the most significant geometric changes and associated vibrational excitation of the 2-butenal product provide a very good representation of the experimental TKER distributions over a wide range of excitation energies and available energies.

2-butenal oxide is similar to its isoprene-derived isomers in having extended π conjugation across the carbonyl oxide and vinyl groups, but differing in the location of a methyl substituent. 2-butenal oxide and MACR-oxide exhibit similar TKER distributions, which are reproduced by the reduced impulsive model, with comparable energies available to O (^{1}D) + carbonyl products. By contrast, photodissociation of MVK-oxide exhibits a notably lower and narrower TKER distribution indicative of greater vibrational activation of the MVK product compared to its isomers. Analysis based on the reduced impulsive model indicates activation of hindered rotation of the methyl group and in-plane methyl rock, originating from a 60° reorientation of the methyl group from MVK-oxide to MVK. Overall, the reduced impulsive model provides significant new insights on the vibrational activation of the aldehyde or ketone products upon photodissociation of Criegee intermediates.

ASSOCIATED CONTENT

Supporting Information

The Supporting Information contains description of synthesis method and isomerization mechanisms, additional electronic spectroscopy calculations and velocity map imaging data, and expanded details for the reduced impulsive model.

Data Availability

The data that support the findings of this study are available within the article and its Supporting Information.

Acknowledgements

This research was supported by the U.S. Department of Energy - Basic Energy Sciences under grant DE-FG02-87ER13792 (MIL). This work utilized the Extreme Science and Engineering Discovery Environment (XSEDE) computer resources, which is supported by the National Science Foundation grant number ACI-1548562 through the allocation TG-CHE190088. MCK is grateful to the NSF (CHE 2102626) for financial support of this research. Partial instrumentation support for the MCK laboratory was provided by the NIH (1S10RR023444, 1S10RR022442, 3R01GM118510-03S1, 3R01GM087605-06S1). Partial support of this research (TNVK) was provided by the National Science Foundation grant number CHE-2003422.

References

1. Sindelarova, K.; Granier, C.; Bouarar, I.; Guenther, A.; Tilmes, S.; Stavrakou, T.; Müller, J. F.; Kuhn, U.; Stefani, P.; Knorr, W., Global data set of biogenic VOC emissions calculated by the MEGAN model over the last 30 years. *Atmos. Chem. Phys.* **2014,** *14*, 9317-9341.
2. Taatjes, C. A.; Shallcross, D. E.; Percival, C. J., Research frontiers in the chemistry of Criegee intermediates and tropospheric ozonolysis. *Phys. Chem. Chem. Phys.* **2014,** *16*, 1704-1718.
3. Khan, M. A. H.; Percival, C. J.; Caravan, R. L.; Taatjes, C. A.; Shallcross, D. E., Criegee intermediates and their impacts on the troposphere. *Environ. Sci.: Process. Impacts* **2018,** *20*, 437-453.
4. Johnson, D.; Marston, G., The gas-phase ozonolysis of unsaturated volatile organic compounds in the troposphere. *Chem. Soc. Rev.* **2008,** *37*, 699-716.
5. Chhantyal-Pun, R.; Khan, M. A. H.; Taatjes, C. A.; Percival, C. J.; Orr-Ewing, A. J.; Shallcross, D. E., Criegee intermediates: Production, detection and reactivity. *Int. Rev. Phys. Chem.* **2020,** *39*, 385-424.
6. Vereecken, L.; Francisco, J. S., Theoretical studies of atmospheric reaction mechanisms in the troposphere. *Chem. Soc. Rev.* **2012,** *41*, 6259-6293.
7. Stephenson, T. A.; Lester, M. I., Unimolecular decay dynamics of Criegee intermediates: Energy-resolved rates, thermal rates, and their atmospheric impact. *Int. Rev. Phys. Chem.* **2020,** *39*, 1-33.
8. Lester, M. I.; Klippenstein, S. J., Unimolecular decay of Criegee intermediates to OH radical products: Prompt and thermal decay processes. *Acc. Chem. Res.* **2018,** *51*, 978-985.
9. Riedel, K.; Lassey, K., Detergent of the atmosphere. *Water. Atmos.* **2008,** *16*, 22-23.
10. Percival, C. J.; Welz, O.; Eskola, A. J.; Savee, J. D.; Osborn, D. L.; Topping, D. O.; Lowe, D.; Utembe, S. R.; Bacak, A.; M c Figgans, G., et al., Regional and global impacts of Criegee intermediates on atmospheric sulphuric acid concentrations and first steps of aerosol formation. *Faraday Discuss.* **2013,** *165*, 45-73.
11. Chhantyal-Pun, R.; Rotavera, B.; McGillen, M. R.; Khan, M. A. H.; Eskola, A. J.; Caravan, R. L.; Blacker, L.; Tew, D. P.; Osborn, D. L.; Percival, C. J., et al., Criegee intermediate reactions with carboxylic acids: A potential source of secondary organic aerosol in the atmosphere. *ACS Earth Space Chem.* **2018,** *2*, 833-842.
12. Nguyen, T. B.; Tyndall, G. S.; Crounse, J. D.; Teng, A. P.; Bates, K. H.; Schwantes, R. H.; Coggon, M. M.; Zhang, L.; Feiner, P.; Milller, D. O., et al., Atmospheric fates of Criegee intermediates in the ozonolysis of isoprene. *Phys. Chem. Chem. Phys.* **2016,** *18*, 10241-10254.
13. Hansen, A. S.; Qian, Y.; Sojdak, C. A.; Kozlowski, M. C.; Esposito, V. J.; Francisco, J. S.; Klippenstein, S. J.; Lester, M. I., Rapid allylic 1,6 H-atom transfer in an unsaturated Criegee intermediate. *J. Am. Chem. Soc.* **2022,** *144*, 5945-5955.
14. Karsili, T. N. V.; Marchetti, B.; Lester, M. I.; Ashfold, M. N. R., Electronic absorption spectroscopy and photochemistry of Criegee intermediates. *Photochem. Photobiol.* **2022**.
15. Liu, T. L.; Zou, M. J.; Caracciolo, A.; Sojdak, C. A.; Lester, M. I., Substituent effects on the electronic spectroscopy of four-carbon Criegee intermediates. *J. Phys. Chem. A* **2022**.
16. Vereecken, L.; Novelli, A.; Taraborrelli, D., Unimolecular decay strongly limits the atmospheric impact of Criegee intermediates. *Phys. Chem. Chem. Phys.* **2017,** *19*, 31599-31612.
17. Vansco, M. F.; Caravan, R. L.; Zuraski, K.; Winiberg, F. A. F.; Au, K.; Trongsiriwat, N.; Walsh, P. J.; Osborn, D. L.; Percival, C. J.; Khan, M. A. H., et al., Experimental Evidence of Dioxole Unimolecular Decay Pathway for Isoprene-Derived Criegee Intermediates. *J. Phys. Chem. A* **2020,** *124*, 3542-3554.
18. Caravan, R. L.; Vansco, M. F.; Au, K.; Khan, M. A. H.; Li, Y.-L.; Winiberg, F. A. F.; Zuraski, K.; Lin, Y.-H.; Chao, W.; Trongsiriwat, N., et al., Direct kinetic measurements and theoretical predictions of an isoprene-derived Criegee intermediate. *Proc. Natl. Acad. Sci.* **2020,** *117*, 9733-9740.
19. Vansco, M. F.; Caravan, R. L.; Pandit, S.; Zuraski, K.; Winiberg, F. A. F.; Au, K.; Bhagde, T.; Trongsiriwat, N.; Walsh, P. J.; Osborn, D. L., et al., Formic acid catalyzed isomerization and adduct

formation of an isoprene-derived Criegee intermediate: Experiment and theory. *Phys. Chem. Chem. Phys.* **2020,** *22*, 26796-26805.

20. Vansco, M. F.; Zuraski, K.; Winiberg, F. A. F.; Au, K.; Trongsiriwat, N.; Walsh, P. J.; Osborn, D. L.; Percival, C. J.; Klippenstein, S. J.; Taatjes, C. A., et al., Functionalized hydroperoxide formation from the reaction of methacrolein-oxide, an isoprene-derived Criegee intermediate, with formic acid: Experiment and theory. *Molecules* **2021,** *26*, 3058.
21. Lin, Y.-H.; Yin, C.; Takahashi, K.; Lin, J. J.-M., Surprisingly long lifetime of methacrolein oxide, an isoprene derived Criegee intermediate, under humid conditions. *Commun. Chem.* **2021,** *4*, 12.
22. Caravan, R. L.; Vansco, M. F.; Lester, M. I., Open questions on the reactivity of Criegee intermediates. *Commun. Chem.* **2021,** *4*, 44.
23. Barber, V. P.; Pandit, S.; Green, A. M.; Trongsiriwat, N.; Walsh, P. J.; Klippenstein, S. J.; Lester, M. I., Four-carbon Criegee intermediate from isoprene ozonolysis: Methyl vinyl ketone oxide synthesis, infrared spectrum, and OH production. *J. Am. Chem. Soc.* **2018,** *140*, 10866-10880.
24. Vansco, M. F.; Marchetti, B.; Trongsiriwat, N.; Wang, G.; Bhagde, T.; Walsh, P. J.; Klippenstein, S. J.; Lester, M. I., Synthesis, electronic spectroscopy and photochemistry of methacrolein oxide: A four carbon unsaturated Criegee intermediate from isoprene ozonolysis. *J. Am. Chem. Soc.* **2019,** *141*, 15058-15069.
25. Cai, J. R.; Su, J. H.; Lee, Y. P., Formation reaction mechanism and infrared spectra of *anti-trans*-methacrolein oxide and its associated precursor and adduct radicals. *Commun. Chem.* **2022,** *5*, 26.
26. Lin, Y. H.; Li, Y. L.; Chao, W.; Takahashi, K.; Lin, J. J., The role of the iodine-atom adduct in the synthesis and kinetics of methyl vinyl ketone oxide—a resonance-stabilized Criegee intermediate. *Phys. Chem. Chem. Phys.* **2020,** *22*, 13603-13612.
27. Vansco, M. F.; Marchetti, B.; Lester, M. I., Electronic spectroscopy of methyl vinyl ketone oxide: A four-carbon unsaturated Criegee intermediate from isoprene ozonolysis. *J. Chem. Phys.* **2018,** *149*, 244309.
28. Sheps, L., Absolute ultraviolet absorption spectrum of a Criegee intermediate CH_2OO. *J. Phys. Chem. Lett.* **2013,** *4*, 4201-4205.
29. Ting, W.-L.; Chen, Y.-H.; Chao, W.; Smith, M. C.; Lin, J. J.-M., The UV absorption spectrum of the simplest Criegee intermediate CH_2OO. *Phys. Chem. Chem. Phys.* **2014,** *16*, 10438-10443.
30. Smith, M. C.; Ting, W.-L.; Chang, C.-H.; Takahashi, K.; Boering, K. A.; Lin, J. J.-M., UV absorption spectrum of the C2 Criegee intermediate CH_3CHOO. *J. Chem. Phys.* **2014,** *141*, 074302.
31. Sheps, L.; Scully, A. M.; Au, K., UV absorption probing of the conformer-dependent reactivity of a Criegee intermediate CH_3CHOO. *Phys. Chem. Chem. Phys.* **2014,** *16*, 26701-26706.
32. Huang, H.-L.; Chao, W.; Lin, J. J.-M., Kinetics of a Criegee intermediate that would survive high humidity and may oxidize atmospheric SO_2. *Proc. Natl. Acad. Sci.* **2015,** *112*, 10857-10862.
33. Lin, Y. H.; Yang, C. H.; Takahashi, K.; Lin, J. J., Kinetics of unimolecular decay of methyl vinyl ketone oxide, an isoprene-derived Criegee intermediate, under atmospherically relevant conditions. *J. Phys. Chem. A* **2020,** *124*, 9375-9381.
34. Beames, J. M.; Liu, F.; Lu, L.; Lester, M. I., Ultraviolet spectrum and photochemistry of the simplest Criegee intermediate CH_2OO. *J. Am. Chem. Soc.* **2012,** *134*, 20045-20048.
35. Liu, F.; Beames, J. M.; Green, A. M.; Lester, M. I., UV spectroscopic characterization of dimethyl- and ethyl-substituted carbonyl oxides. *J. Phys. Chem. A* **2014,** *118*, 2298-2306.
36. Liu, F.; Beames, J. M.; Petit, A. S.; McCoy, A. B.; Lester, M. I., Infrared-driven unimolecular reaction of CH_3CHOO Criegee intermediates to OH radical products. *Science* **2014,** *345*, 1596-1598.
37. Liu, F.; Beames, J. M.; Lester, M. I., Direct production of OH radicals upon CH overtone activation of $(CH_3)_2COO$ Criegee intermediates. *J. Chem. Phys.* **2014,** *141*, 234312.
38. Beames, J. M.; Liu, F.; Lu, L.; Lester, M. I., UV spectroscopic characterization of an alkyl substituted Criegee intermediate CH_3CHOO. *J. Chem. Phys.* **2013,** *138*, 244307.
39. Wang, G.; Liu, T.; Caracciolo, A.; Vansco, M. F.; Trongsiriwat, N.; Walsh, P. J.; Marchetti, B.; Karsili, T. N. V.; Lester, M. I., Photodissociation dynamics of methyl vinyl ketone oxide: A four-

carbon unsaturated Criegee intermediate from isoprene ozonolysis. *J. Chem. Phys.* **2021,** *155*, 174305.

40. Eppink, A. T. J. B.; Parker, D. H., Velocity map imaging of ions and electrons using electrostatic lenses: Application in photoelectron and photofragment ion imaging of molecular oxygen. *Rev. Sci. Instrum.* **1997,** *68*, 3477-3484.
41. Lehman, J. H.; Li, H.; Beames, J. M.; Lester, M. I., Communication: Ultraviolet photodissociation dynamics of the simplest Criegee intermediate CH_2OO. *J. Chem. Phys.* **2013,** *139*, 141103.
42. Li, H.; Fang, Y.; Beames, J. M.; Lester, M. I., Velocity map imaging of O-atom products from UV photodissociation of the CH_2OO Criegee intermediate. *J. Chem. Phys.* **2015,** *142*, 214312.
43. Li, H.; Fang, Y.; Kidwell, N. M.; Beames, J. M.; Lester, M. I., UV photodissociation dynamics of the CH_3CHOO Criegee intermediate: Action spectroscopy and velocity map imaging of O-atom products. *J. Phys. Chem. A* **2015,** *119*, 8328-8337.
44. Vansco, M. F.; Li, H.; Lester, M. I., Prompt release of O ^{1}D products upon UV excitation of CH_2OO Criegee intermediates. *J. Chem. Phys.* **2017,** *147*, 013907.
45. Esposito, V. J.; Liu, T.; Wang, G.; Caracciolo, A.; Vansco, M. F.; Marchetti, B.; Karsili, T. N. V.; Lester, M. I., Photodissociation dynamics of CH_2OO on multiple potential energy surfaces: Experiment and theory. *J. Phys. Chem. A* **2021,** *125*, 6571-6579.
46. Pratt, S. T.; Dehmer, P. M.; Dehmer, J. L., Double-resonance spectroscopy of transitions between autoionizing levels of atomic oxygen. *Phys. Rev. A* **1991,** *43*, 4702-4711.
47. Garcia, G. A.; Nahon, L.; Powis, I., Two-dimensional charged particle image inversion using a polar basis function expansion. *Rev. Sci. Instrum.* **2004,** *75*, 4989-4996.
48. Dooley, K. S.; Geidosch, J. N.; North, S. W., Ion imaging study of IO radical photodissociation: Accurate bond dissociation energy determination. *Chem. Phys. Lett.* **2008,** *457*, 303-306.
49. Frisch, M. J.; Trucks, G. W.; Schlegel, H. B.; Scuseria, G. E.; Robb, M. A.; Cheeseman, J. R.; Scalmani, G.; Barone, V.; Petersson, G. A.; Nakatsuji, H., et al. *Gaussian 16 Rev. A.03, Wallingford CT* Wallingford, CT, 2016.
50. McCoy, J. C.; Marchetti, B.; Thodika, M.; Karsili, T. N. V., A simple and efficient method for simulating the electronic absorption spectra of Criegee intermediates: Benchmarking on CH_2OO and CH_3CHOO. *J. Phys. Chem. A* **2021,** *125*, 4089-4097.
51. Werner, H.-J.; Knowles, P. J.; Knizia, G.; Manby, F. R.; Schütz, M.; Celani, P.; Györffy, W.; Kats, D.; Korona, T.; Lindh, R., et al. *MOLPRO 2020.1, A package of ab initio programs, see www.molpro.net*, 2020.
52. Werner, H.-J.; Knowles, P. J.; Manby, F. R.; Black, J. A.; Doll, K.; Heßelmann, A.; Kats, D.; Köhn, A.; Korona, T.; Kreplin, D. A., et al., The Molpro quantum chemistry package. *J. Chem. Phys.* **2020,** *152*, 144107.
53. Werner, H.-J.; Knowles, P. J.; Knizia, G.; Manby, F. R.; Schütz, M., Molpro: a general-purpose quantum chemistry program package. *Wiley Interdiscip. Rev. Comput. Mol. Sci.* **2012,** *2*, 242-253.
54. McCoy, J. C.; Leger, S. J.; Frey, C. F.; Vansco, M. F.; Marchetti, B.; Karsili, T. N. V., Modeling the conformer-dependent electronic absorption spectra and photolysis rates of methyl vinyl ketone oxide and methacrolein oxide. *J. Phys. Chem. A* **2022,** *126*, 485-496.
55. Mai, S.; Marquetand, P.; González, L., Nonadiabatic dynamics: The SHARC approach. *Wiley Interdiscip. Rev. Comput. Mol. Sci.* **2018,** *8*, e1370.
56. Richter, M.; Marquetand, P.; González-Vázquez, J.; Sola, I.; González, L., SHARC: *ab initio* molecular dynamics with surface hopping in the adiabatic representation including arbitrary couplings. *J. Chem. Theory Comput.* **2011,** *7*, 1253-1258.
57. Mai, S.; Richter, M.; Heindl, M.; Menger, M.; Atkins, A.; Ruckenbauer, M.; Plasser, F.; Ibele, L.; Kropf, S.; Oppel, M. *SHARC: Surface hopping including arbitrary couplings—Program package for non-adiabatic dynamics, see sharc-md.org*, 2014.
58. Towns, J.; Cockerill, T.; Dahan, M.; Foster, I.; Gaither, K.; Grimshaw, A.; Hazlewood, V.; Lathrop, S.; Lifka, D.; Peterson, G. D., et al., XSEDE: Accelerating scientific discovery. *Comput. Sci. Eng.* **2014,** *16*, 62-74.

59. Dawes, R.; Jiang, B.; Guo, H., UV absorption spectrum and photodissociation channels of the simplest Criegee intermediate (CH_2OO). *J. Am. Chem. Soc.* **2015,** *137*, 50-3.
60. Bai, S.; Mansour, R.; Stojanovic, L.; Toldo, J. M.; Barbatti, M., On the origin of the shift between vertical excitation and band maximum in molecular photoabsorption. *J. Mol. Model* **2020,** *26*, 107.
61. Herzberg, G., *Molecular Spectra and Molecular Structure, Volume III: Electronic Spectra and Electronic Structure of Polyatomic Molecules*. Krieger Publishing Company: 1991; Vol. III.
62. Schinke, R., *Photodissociation Dynamics*. Cambridge University Press: 1993.
63. Esposito, V. J.; Werba, O.; Bush, S. A.; Marchetti, B.; Karsili, T. N. V., Insights into the ultrafast dynamics of CH_2OO and CH_3CHOO following excitation to the bright $^1\pi\pi^*$ state: The role of singlet and triplet states. *Photochem. Photobiol.* **2022,** *98*, 763-772.
64. Lin, Y. H.; Takahashi, K.; Lin, J. J., Absolute photodissociation cross sections of thermalized methyl vinyl ketone oxide and methacrolein oxide. *Phys. Chem. Chem. Phys.* **2022,** *24*, 10439-10450.
65. Nakajima, M.; Endo, Y., Communication: Determination of the molecular structure of the simplest Criegee intermediate CH_2OO. *J. Chem. Phys.* **2013,** *139*, 101103.
66. Oelichmann, H.-J.; Bougeard, D.; Schrader, B., Coupled calculation of vibrational frequencies and intensities: Part VI. IR and Raman spectra of crotonaldehyde, methacrolein and methyl-vinylketone. *J. Mol. Struct.* **1981,** *77*, 179-194.
67. Barker, J. R.; Nguyen, T. L.; Stanton, J. F.; Aieta, C.; Ceotto, M.; Gabas, F.; Kumar, T. J. D.; Li, C. G. L.; Lohr, L. L.; Maranzana, A., et al. *MultiWell-2019 Software Suite*, University of Michigan: Ann Arbor, Michigan, USA, 2019.

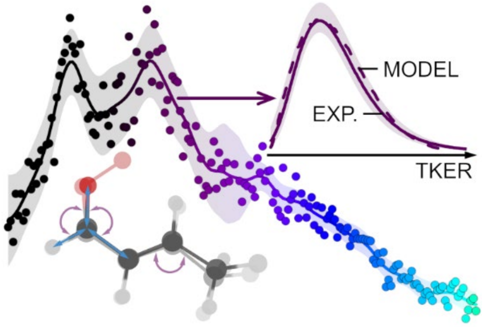

TOC Graphic